

Article

Modified FMCW Scheme for Improved Ultrasonic Positioning and Ranging of Unmanned Ground Vehicles at Distances < 50 mm

Stefano Laureti ^{1,*}, Marco Mercuri ¹, David A. Hutchins ², Felice Crupi ¹ and Marco Ricci ¹

¹ Department of Informatics, Modelling, Electronics and Systems Engineering, University of Calabria, Via Pietro Bucci, Arcavacata, 87036 Rende, CS, Italy

² School of Engineering, University of Warwick, Coventry CV4 7AL, UK

* Correspondence: stefano.laureti@unical.it

Abstract: Unmanned ground vehicles (UGVs) find extensive use in various applications, including that within industrial environments. Efforts have been made to develop cheap, portable, and light-ranging/positioning systems to accurately locate their absolute/relative position and to automatically avoid potential obstacles and/or collisions with other drones. To this aim, a promising solution is the use of ultrasonic systems, which can be set up on UGVs and can potentially output a precise reconstruction of the drone's surroundings. In this framework, a so-called frequency-modulated continuous wave (FMCW) scheme is widely employed as a distance estimator. However, this technique suffers from low repeatability and accuracy at ranges of less than 50 mm when used in combination with low-resource hardware and commercial narrowband transducers, which is a distance range of the utmost importance to avoid potential collisions and/or imaging UGV surroundings. We hereby propose a modified FMCW-based scheme using an ad hoc time-shift of the reference signal. This was shown to improve performance at ranges below 50 mm while leaving the signal unaltered at greater distances. The capabilities of the modified FMCW were evaluated numerically and experimentally. A dramatic enhancement in performance was found for the proposed FMCW with respect to its standard counterpart, which is very close to that of the correlation approach. This work paves the way for the future use of FMCWs in applications requiring high precision.

Keywords: ultrasounds; FMCW; correlation; unmanned ground vehicles; ranging; positioning



Citation: Laureti, S.; Mercuri, M.; Hutchins, D.A.; Crupi, F.; Ricci, M. Modified FMCW Scheme for Improved Ultrasonic Positioning and Ranging of Unmanned Ground Vehicles at Distances < 50 mm. *Sensors* **2022**, *22*, 9899. <https://doi.org/10.3390/s22249899>

Academic Editors: Massimo Merenda, Riccardo Carotenuto and Andrey V. Savkin

Received: 24 September 2022

Accepted: 13 December 2022

Published: 15 December 2022

Publisher's Note: MDPI stays neutral with regard to jurisdictional claims in published maps and institutional affiliations.



Copyright: © 2022 by the authors. Licensee MDPI, Basel, Switzerland. This article is an open access article distributed under the terms and conditions of the Creative Commons Attribution (CC BY) license (<https://creativecommons.org/licenses/by/4.0/>).

1. Introduction

As the use of unmanned ground vehicles (UGVs) and unmanned aerial vehicles (UAVs), also known as “drones” is currently increasing, extended efforts have been made to develop systems for tracking and determining their position, both outdoors and indoors. While multiple UGVs and drones can be tracked and located outdoors using global navigation satellite system (GNSS) receivers, the accuracy provided is often insufficient at distances below 1000 mm, and this is dramatically reduced in indoor environments due to the lack of satellite coverage [1].

Existing measurement technologies for indoor tracking and positioning include wireless sensor networks [2,3], radio frequency-based systems [4–7], video-based localization systems [8,9], infrared positioning systems [10–12], wireless local area networks [13–15] and Bluetooth-based systems [16,17]. The reader is referred to, e.g., Mainetti et al. [18] or to Koyuncu et al. [19], for a thorough comparison of such measurement approaches in terms of hardware requirements, cost, working range, measurement resolution, and repeatability.

In addition, ultrasonic transmitters (Tx) and receivers (Rx) can be fixed to both UGVs and UAVs as a reliable, light, and inexpensive solution. They can be used to accurately estimate the distance from/to a specific cartesian origin to track their relative positions, and to map the surrounding environment [20,21]. It is worth noting that UGVs are often used

within industrial environments; therefore, the use of ultrasound for range and positioning applications instead of electromagnetic methods is beneficial for avoiding unwanted interaction with other electromagnetic sources or metal parts and structures [22], especially when these are aimed at being used for application with high accuracy.

The basis of an ultrasonic ranging system is the accurate and rapid estimation of the time-of-flight (*TOF*), which is the time taken for the ultrasonic stimulus to travel from the Tx to the Rx. The distance between the Tx and Rx, i.e., the distance either between drones or from a drone to a given target/obstacle, is then inferred from the *TOF* using the speed of sound in air, which is 343 m/s at room temperature [23]. However, an accurate estimation of the *TOF* relies on the use of advanced signal conditioning and post-processing algorithms. In such cases, the use of frequency-modulated swept-sine “chirp” signals as the excitation waveform has been shown to be of great help for *TOF* estimation, especially in poor signal-to-noise ratio (SNR) conditions [24]. However, this is difficult to use when inexpensive narrowband ultrasonic transducers and low-cost hardware are employed.

Different post-processing strategies have been developed to further improve the range estimation capabilities when using such coded signals, among which the correlation method, also known as pulse-compression (PuC) [25,26], and the frequency-modulated continuous waveform (FMCW) [27–29] are the most frequently employed. The former provides the highest accuracy and repeatability of *TOF* estimation, although it is based on a convolution procedure and, thus, requires relatively powerful hardware to be correctly performed. The latter relaxes several hardware constraints at the cost of reduced accuracy and repeatability, especially when using narrowband transducers and low-cost hardware.

In general, correlation-based estimation is the best choice for ranging and positioning applications [30]. However, when cheap, light, portable, and low-power ultrasonic ranging and positioning systems are aimed at being set up, e.g., on drones, FMCWs can be a trade-off solution between the design constraints and the *TOF* estimation accuracy and repeatability.

Several studies have focused on reducing the computational requirements of the correlation, to explore alternative post-processing strategies, and to compare the capabilities of the correlation and the FMCW methods. Barshan [31] compared four different methods for distance estimation in the range of 100–5000 mm, i.e., simple thresholding, curve-fitting, sliding-window, and correlation, and found that, whereas the correlation is a theoretical optimal in terms of bias error, standard deviation, total error, and robustness to noise, the other algorithms offer enough performances at a much lower computational cost. Huang et al. [32] used binary frequency shift-keyed signals as excitation waveforms plus phase detection to improve *TOF* estimation in the range of 1000–6000 mm and found a range accuracy within ± 0.05 mm. Hazas and Hopper [33] prototyped a broadband “Dolphin” transmitter and receiver unit to overcome the limitation of using narrowband ultrasonic transducers in the range of 500–2500 mm. Saad et al. [34] explored the use of wideband frequency-hopping spread spectrum techniques in combination with a minimum variance search technique to correct the error in correlation-based *TOF* measurement, yielding an improvement in the estimations within the range 500–7000 mm. Jackson et al. [35] compared several time-domain approaches with their frequency-domain counterparts, focusing especially on the accuracy and repeatability of the *TOF* measurements. Additionally, the use of a hybrid time-frequency domain and biologically inspired models was investigated for measurement in the range of 100–1000 mm. Ronkin et al. [36] introduced a novel approach for FMCW-based *TOF* estimators relying on a heterodyne scheme, which showed improved performances over the above-reported processing algorithms. Efforts have also been made to make ultrasonic FMCW-based systems highly portable, light, and based on low-power hardware (see, for instance, Berkol et al. [37] or De Angelis et al. [38]) and to combine the ultrasound ranging with infrared technology to improve the overall accuracy [39] in the range of 50–1000 mm and 500–1400 mm, respectively.

It can be noticed from the literature that few authors have used ultrasonic FMCWs for very small *TOF* estimation at distances below 50 mm in air. In fact, FMCW suffers from

very low accuracy and repeatability when the Tx and Rx are very close together with respect to correlation-based estimation, especially when a relatively-low sampling frequency and narrowband transducers are employed [40]. The *TOF* resolution lower bound for the FMCW technique is $1/B$, with B being the transducer bandwidth [28,30]. However, being able to effectively exploit the ultrasonic FMCW technique, even for very close targets, would be of interest for the tracking and positioning of UGVs and drones within a fleet to avoid potential collisions and to faithfully map their surrounding environment. It is worth mentioning that ultrasound is widely used in a plethora of different applications, such as nondestructive testing and evaluation [41–43], sonochemistry [44], medical treatment [45–48], and imaging [49], so several ultrasonic ranges and positioning schemes benefit from research in these areas.

This paper introduces a modified FMCW measurement scheme that dramatically improves *TOF* estimation for distances < 50 mm, i.e., below the theoretical limit of the $1/B$ of the current setup, which can be implemented via simple and portable signal generation and acquisition hardware.

The capabilities of such an approach will be evaluated numerically and experimentally considering both the features of suitable hardware and the central frequency/bandwidth of widely-available ultrasonic sensors, such as the one commonly employed in parking sensors. By establishing ad hoc figures of merit, the standard and modified FMCW-based approaches are compared to the correlation-based algorithm in terms of accuracy and repeatability for several different distances in air and different SNR levels so as to mimic different attenuation levels. Additionally, a three-point parabolic fit [30] will be implemented on the estimated *TOFs* to simulate the results of using a phase-locked loop (PLL) in a frequency-demodulation configuration for a precise reading of the frequency beat value [50].

The paper is organized as follows. Section 2 details the features of the simulated hardware and transducers; the theory and working principle of the correlation and standard FMCW methods are discussed in Section 3, together with the modified FMCW scheme proposed here; Section 4 explains the numerical simulation procedure in detail and contains a thorough description of the figures of merit. The numerical and experimental results are shown and discussed in Section 5. Section 6 draws up conclusions and addresses potential future work.

2. Detail of the Simulated Hardware and Setup

A plethora of signal generators, digital-to-analog (DACs) and analog-to-digital (ADCs) converters, and transducers are available in the market to set up ultrasonic ranging and positioning systems. However, the choice of the equipment specified below is thought to be suitable for enabling the proposed FMCW measurement scheme to be implemented using inexpensive and lightweight hardware. In fact, while the former aspect is, in general, related to the available budget, the choice of lightweight equipment is beneficial to fully exploit the potential of a given UAV. In order to gain more insight, Table 1 shows an accepted taxonomy of UAVs [51]. It can be noticed that micro, mini, and even small UAVs will benefit from the minimization of hardware weight, as both their endurance and payload can be maintained close to the nominal values. Note that the same rationale holds for UGVs.

To this aim, the specifics of a Digilent Analog Discovery 2 (Digilent—National Instrument, Austin, TX, USA) have been simulated here, and the same hardware was used for the experimental activity. This device has a nominal weight of 450 g and a cost of less than USD 400. It provides two DAC arbitrary waveform generators (AWGs) that can be driven at a maximum output voltage of 10 V peak-to-peak, two ADCs channels with 14 bits of resolution, and a maximum buffer of 8000 samples for generating/acquiring the signals at the sampling frequencies f_{ADC} and f_{DAC} , respectively, at up to 100 MSamples/s. Note that the chosen f_{ADC} and f_{DAC} values are much lower than the maximum value, i.e., 500 kSamples/s, so as to allow more inexpensive hardware to be chosen if required in the future.

Table 1. Classification of UAVs.

Category	Weight (kg)	Operating Altitude (m)	Nominal Endurance (h)	Payload (kg)
Micro	<2	<140	<1	<1
Mini	2–25	<1000	2–8	<10
Small	25–150	<1700	4–12	<50
Medium	150–600	<3300	8–20	<200
Large/Tactical	>600	>3300	>20	>200

Concerning the ultrasonic transducers, a pair of Murata MA40S4S transducers (Murata Manufacturing Co., Ltd., Kyoto, Japan) were chosen for study. These are optimized for indoor sensing purposes and have a 7.1 mm diameter active element size, a resonance central frequency f_c equal to 40 kHz, and a -3 dB bandwidth B equal to 5 kHz, all for a cost of less than USD 6 and a weight of about 30 g each.

A sketch of the possible implementation of this hardware onto the top/bottom surface of a UGV is depicted in Figure 1.

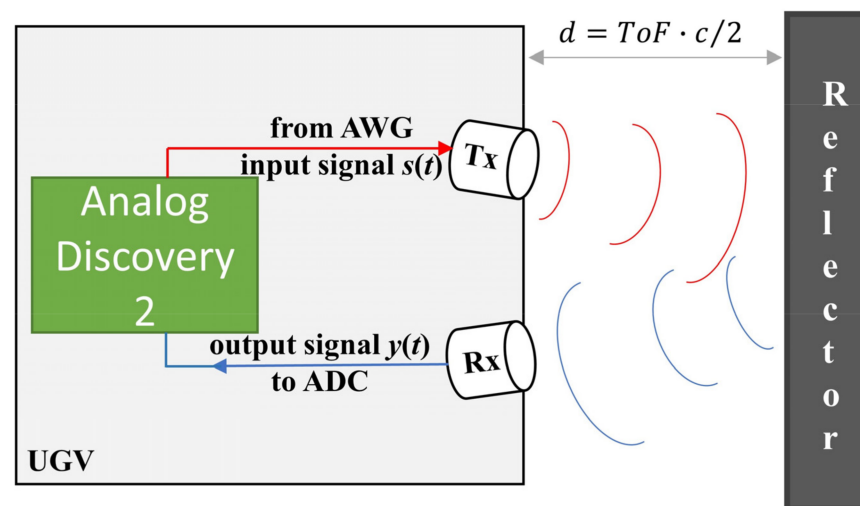
**Figure 1.** A sketch of the simulated ultrasonic ranging and positioning system.

Figure 1 shows that measuring the distance d between a potential sound reflector close to the UGV, e.g., other UGVs or an obstacle, relies on the accurate estimation of TOF from the output signal $y(t)$, with TOF being the time taken by the input ultrasonic signal $s(t)$ to travel from the Tx to the Rx after reflection from an object. Once the TOF is estimated, the distance d is obtained using Equation (1).

$$d = \frac{TOF \cdot c}{2}. \quad (1)$$

Note that a change in air temperature would result in a change in the speed of sound, c , hence influencing the correct estimation of the distance. However, this detrimental effect can be considered negligible when relatively-low TOF values are being estimated, e.g., for $d < 50$ mm, as in the present case.

Different excitation signals, $s(t)$, can be practically employed for estimating TOF , such as simple pulsed excitation, pseudo-noise and chirp signals, stepped-frequency continuous wave signals, etc. However, chirp signals are very often used in ultrasonic positioning and ranging applications for their design flexibility and beneficial features. The next sections will highlight the benefit of such an approach with respect to a simple pulsed excita-

tion, especially in correlation- and FMCW-based schemes in combination with relatively low peak-to-peak input voltages.

3. Theoretical Background

3.1. Linear Swept-Frequency Chirp Signal

The use of frequency-modulated coded signals is well-established in several ultrasonic applications, including ultrasonic-based range and positioning systems [52]. In fact, chirp signals can be easily designed so as to cope with the useful transducer's bandwidth for an arbitrary duration, and they inherently establish a relationship between time and frequency, thus giving a unique advantage in both correlation- and FMCW-based estimators. On top of these, the chirp autocorrelation function is δ -like, which is of the utmost importance in correlation-PuC measurement schemes, as explained in detail in the next subsections. The general formulation of a chirp signal, $s(t)$, is reported in Equation (2).

$$s(t) = \text{Re}\left[e^{2\pi i\left(f_c t + \frac{B}{2} \int_0^t x(\tau) d\tau\right)}\right] = \text{Re}\left[e^{i\Phi(t)}\right], \quad (2)$$

with $\Phi(t)$ being a nonlinear phase function of the time, $x(\tau)$ is a monotonically increasing, smooth modulating signal taking values in $[-1,1]$, $t \in [0, T]$ so that T is the chirp time duration, $f_c = \frac{f_1+f_2}{2}$ is the central frequency of the chirp, and $B = f_2 - f_1$ is the bandwidth, with f_1 and f_2 being the start and stop frequency of the chirp, respectively; Re stands for the real part operator. The instantaneous frequency of $s(t)$ is defined as $f_{inst}(t) = \frac{1}{2\pi} \frac{d\Phi(t)}{dt}$. If the phase $\Phi(t)$ is chosen so as to be a quadratic function of the time, as per Equation (3) [42], then:

$$\Phi(t) = 2\pi\left(f_c t + \frac{B}{2T} t^2 - \frac{B}{2} t\right) = 2\pi\left(f_1 t + \frac{B}{2T} t^2\right), \quad (3)$$

then, a linear chirp is obtained:

$$s(t) = \text{Re}\left[e^{2\pi i\left(f_1 t + \frac{B}{2T} t^2\right)}\right], \quad (4)$$

whose $f_{inst}(t)$ in $t \in [0, T]$ is:

$$f_{inst}(t) = f_1 + \frac{B}{T} t = f_1 + k_f t, \quad (5)$$

with $k_f = \frac{B}{T}$.

Figure 2a shows an example of the $f_{inst}(t)$ for a linear chirp signal with $f_1 = 47.5$ kHz, $f_2 = 52.5$ kHz, and $T = 4$ ms, while Figure 2b depicts its frequency spectrum obtained using the fast Fourier transform (FFT) algorithm.

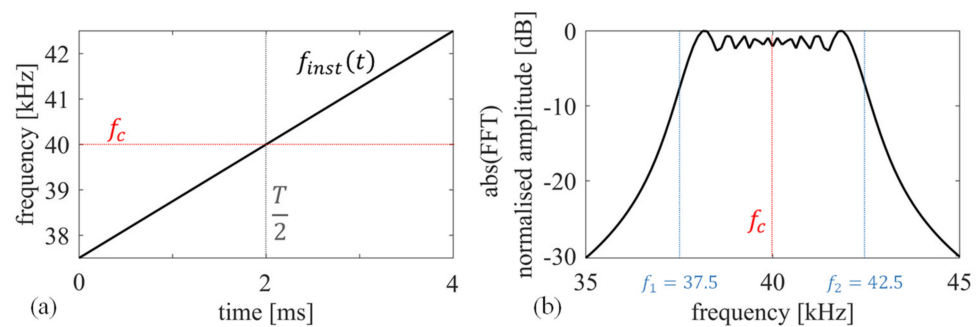


Figure 2. (a) Time-frequency handling for a chirp signal, sweeping from 37.5 kHz to 42.5 kHz in 4 ms, and (b) its frequency spectrum.

Note that these chirp characteristics are used throughout the manuscript, as they align with the chosen transducer's nominal bandwidth.

3.2. Pulse-Compression/Correlation Basic Theory

PuC is a measurement technique that is largely employed to experimentally estimate the impulse response, $h(t)$, of a linear time-invariant (LTI) system, which is highly beneficial when dealing with poor SNR values.

PuC uses a coded excitation, $s(t)$, and another signal, $\Psi(t)$, the so-called matched-filter, such that their convolution (*) approximates the Dirac's delta function, $\delta(t)$, so that $[s * \Psi](t) = \tilde{\delta}(t) \sim \delta(t)$. The impulse response, $h(t)$, is thus estimated by exciting the LTI system with the signal $s(t)$ and then convolving the system output $y(t)$ with $\Psi(t)$. Note that the linear chirp signal described in Section 3.1 is largely employed in PuC-based measurements, as its autocorrelation function is $\tilde{\delta}(t)$.

PuC can be mathematically demonstrated considering an output signal $y(t)$, physically resulting from the convolution between the input signal $s(t)$ and the system's impulse response $h(t)$, on which is superimposed an additive white Gaussian noise (AWGN) $e(t)$: $y(t) = [h * s](t) + e(t)$, with $\Psi(t)$ and $e(t)$ assumed to be uncorrelated. In practical terms, $s(t)$ is the chirp signal generated from the Tx, whilst $y(t)$ is just the signal acquired from the Rx ultrasonic transducer and is digitized via the ADC.

An estimate, $\tilde{h}(t)$, of the impulse response $h(t)$ is then obtained, convolving $y(t)$ with the matched filter, $\Psi(t)$:

$$\tilde{h}(t) = [y * \Psi](t) = h(t) * \underbrace{[s * \Psi](t)}_{\sim \delta(t)} + [e * \Psi](t) \sim [h * \delta](t) + \tilde{e}(t) = h(t) + \tilde{e}(t), \quad (6)$$

with $\tilde{e}(t)$ also being AWGN but with lower energy than $e(t)$, hence resulting in an increased SNR level. Note that, in the case of a periodic excitation, Equation (6) is a *cyclic* correlation and can be easily implemented in the frequency domain as per Equation (7):

$$\tilde{h}[n] = DFT^{-1} \left\{ DFT\{y[n]\} \times (DFT\{s[n]\})^f \right\}, \quad (7)$$

where digital signals have also been considered, hence *DFT* stands for discrete fourier transform, and “*f*” for complex-conjugate. The reader is referred to Hutchins et al. [53] or to Misaridis et al. [54] for a thorough description of the PuC algorithm in ultrasonic applications. The main advantage of using the PuC scheme in combination with chirp signals is that the SNR of the estimated $\tilde{h}(t)$ can be increased with respect to, e.g., the easier use of a standard pulsed excitation while assuring the same or even better range resolution. This beneficial effect happens when the energy of the chirp signal is larger than that of a standard pulsed excitation and the same, or a larger bandwidth is excited by the chirp. It should be noted that hardware constraints play a key role here: the maximum time duration of both the chirp T_{chirp} and of a pulse signal T_{pulse} are constrained by the available buffer size and the f_{DAC} of Analog Discovery 2, i.e., T , and so is the maximum amplitude (10 V peak-to-peak). On top of that, the available B is dictated by the ultrasonic transducers, in this case, 5 kHz. However, for a standard pulse of duration T_{pulse} , the excited bandwidth is $B \propto \frac{1}{T_{pulse}}$, so that T_{pulse} is very unlikely to be equal in value to T . The same does not hold for the chirp signal, as the duration, T_{chirp} , is not directly constrained by B , and its duration can be as long as the available T of the hardware, see Equation (5). If the pulse amplitude is constant and equal to A_{pulse} , the pulse energy is $E_{pulse} = A_{pulse} T_{pulse} = \frac{A_{pulse}}{B}$ while the chirp energy is $E_{chirp} = A_{chirp} T_{chirp}$. Choosing $A_{pulse} = A_{chirp} = 10$ V, the maximum available SNR gain is

$$SNR_{gain} = \frac{SNR_{PuC-Chirp}}{SNR_{pulse}} = \frac{E_{chirp}}{E_{pulse}} = \frac{A_{chirp}}{A_{pulse}} \cdot T \cdot B = T \cdot B \quad (8)$$

Thus, the available SNR gain is proportional to the time-bandwidth product ($T \cdot B$) of the coded signal [55], hence the use of a chirp signal instead of a simple pulse.

It has been found that, in terms of SNR, the best choice for the matched filter is simply $\Psi(t) = s(-t)$ [56], i.e., employing the time reversal of the input signal as the matched filter.

Thus, Equations (6) and (7) are simply a correlation between the received signal and the matched filter, where the maximum amplitude of the correlation output is at $t = 0$ if no delay between the two signals is found, i.e., $ToF = 0$ s. When a reflector is placed at $d > 0$ mm, then the correlation peak of $\tilde{h}(t)$ obtained from Equation (6) shifts accordingly. This concept is shown in Figure 3, where three waveforms ($y(t)$) have been time-shifted so as to mimic the reflectors at distances equal to $d_1 = 300$ mm, $d_2 = 600$ mm, and $d_3 = 900$ mm, using the same chirp parameters as in Figure 2. Note that for the sake of clarity, no sound attenuation is here taken into account. The different $ToFs$ are, thus, estimated via the correlation-based approach as per Equation (9):

$$TOF = \underset{t}{\operatorname{argmax}} [\tilde{h}(t)], \quad (9)$$

thus, obtaining $ToF_{d_1}^{Corr}$, $ToF_{d_2}^{Corr}$, $ToF_{d_3}^{FMCW}$ of 0.874 ms, 1.750 ms, and 2.624 ms, respectively. By substituting the estimated $ToFs$ into Equation (1), distances of 299.78 mm, 600.25 mm, and 900.03 mm are obtained.

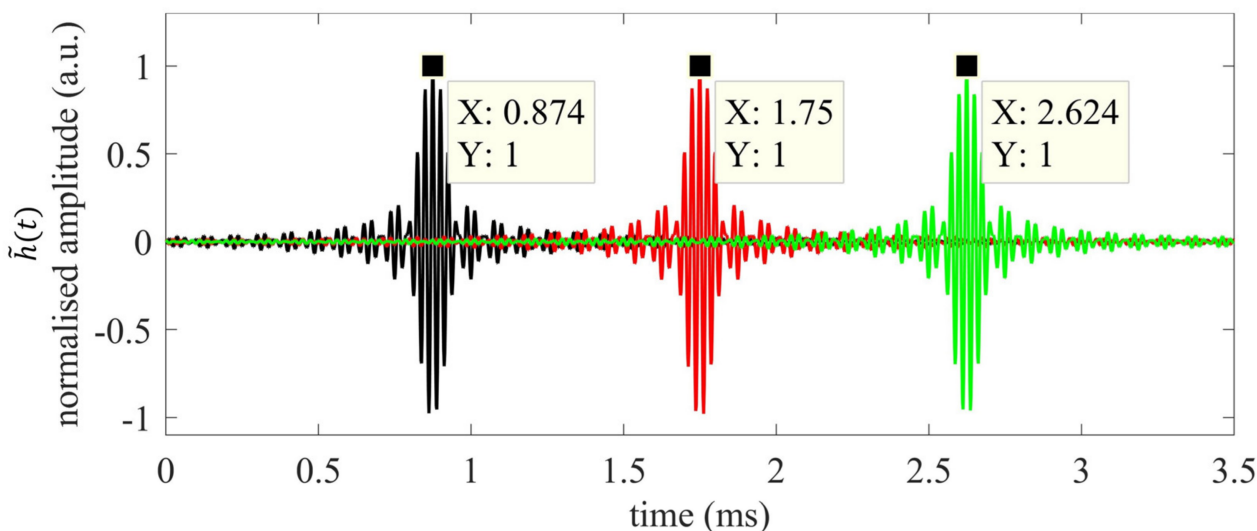


Figure 3. Simulated crosscorrelation outputs for reflectors at $d_1 = 300$ mm (black), $d_2 = 600$ mm (red), and $d_3 = 900$ mm (green) from the transducer pair.

It is worth noting that the estimated distances are slightly different from the simulated ones, and this error becomes larger for relatively low distances. Nevertheless, the error can be reduced by using several post-processing techniques, such as interpolation, so as to better estimate the sample/time position of the correlation peak. These can be applied both for correlation- and FMCW-based estimation. In this paper, only a parabolic interpolation procedure will be exploited—the idea here is to propose a workaround based on a very simple approach that can be directly implemented onboard with simple hardware and without using any additional postprocessing. The interested reader is referred to, e.g., Svilaonis et al. [30], for details of such post-processing and for a thorough overview of the influence of the hardware parameters on the error.

3.3. FMCW Basic Theory

In FMCW-based estimation, the Tx is excited via a periodic chirp signal—at least two periods are needed— $\bar{s}(t)$, and the Rx receives the output $\bar{y}(t)$ after being reflected from a potential reflector. In the ideal noise-free situation, $\bar{y}(t)$ can be assumed to be just a shifted replica of $\bar{s}(t)$, $\bar{y}(t) = \bar{s}(t - \Delta t)$. In order to retrieve the ToF value, $\bar{y}(t)$ is multiplied by $\bar{s}(t)$, thus obtaining a periodically mixed signal $\bar{\chi}(t)$ that contains a beat tone whose frequency

is strictly related to the time shift between the Tx and Rx signals. In fact, if $\Delta t > 0$, then $\bar{s}(t)$ and $\bar{y}(t)$ have different values for instantaneous frequency, $f_{inst}(t)$, and a beat frequency is produced by mixing them up [57]. In order to gain a better insight into this, Figure 4 shows a sketch of the FMCW basic working principle.

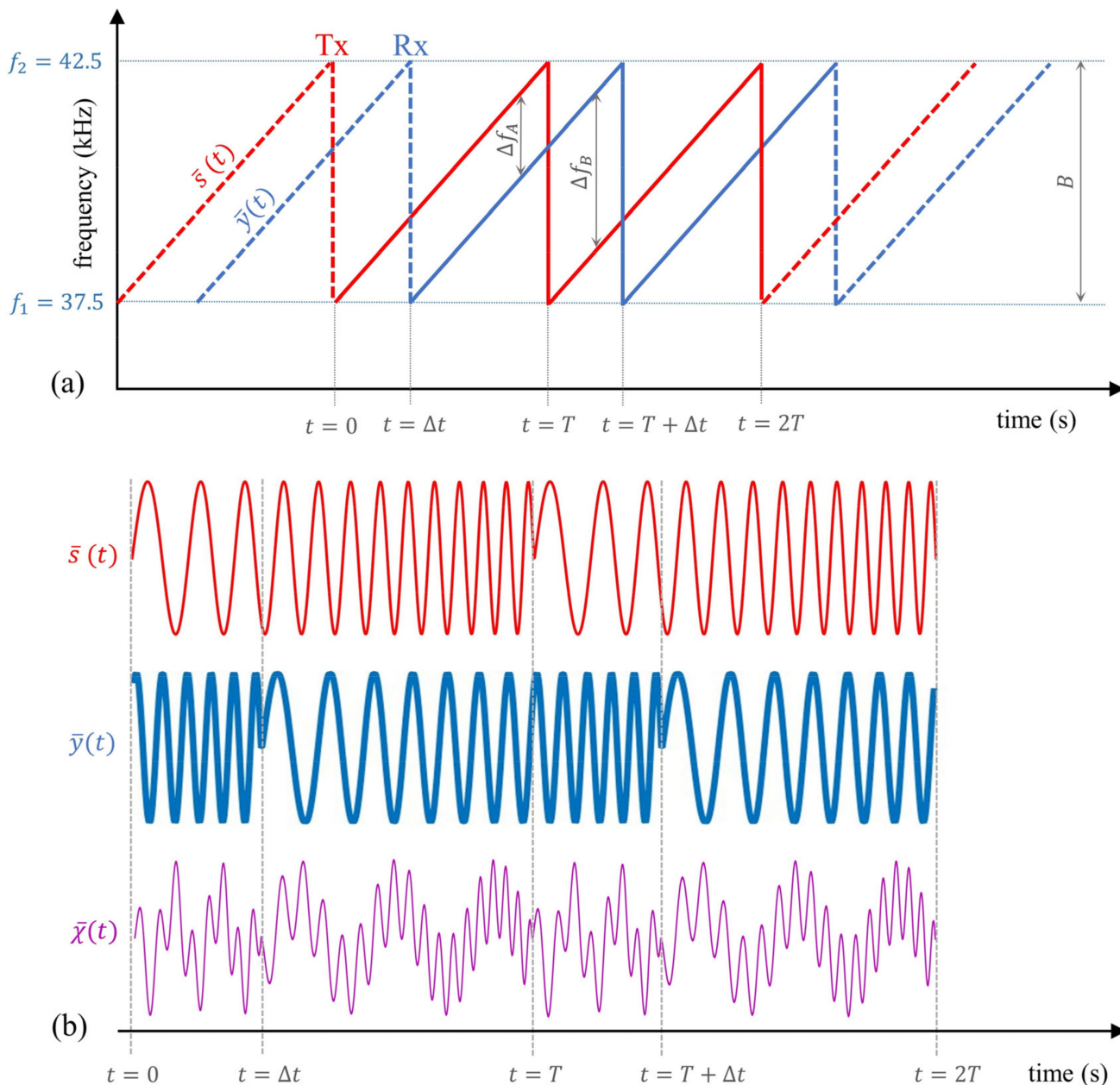


Figure 4. (a) $\bar{s}(t)$ (red) and $\bar{y}(t)$ (blue) signals' $f_{inst}(t)$. Note that $\bar{y}(t)$ is time-shifted (Δt) replica of the transmitted signal $\bar{s}(t)$; (b) an example of the mixed output signal, $\bar{x}(t)$ (purple).

Figure 4a shows that a time delay, Δt , between $\bar{x}(t)$ and $\bar{y}(t)$ results in the two values for the instantaneous frequency differences Δf_A and Δf_B in a single period T since a fictitious time shift $\bar{\Delta t} = (T - \Delta t)$ appears due to the periodic nature of the signals. Thus, Δf_A and Δf_B are equal to

$$\begin{aligned} \Delta f_A &= k_f \Delta t, \\ \Delta f_B &= k_f \bar{\Delta t} = k_f (T - \Delta t) = B - \Delta f_A. \end{aligned} \tag{10}$$

Hence, the delay Δt can be estimated by measuring Δf_a and/or Δf_b through a Fourier analysis applied to $\bar{\chi}(t)$.

In order to understand how this is possible, the nature of the mixed signal $\bar{\chi}(t)$ must be analyzed in more detail. By considering Equation (4), and a single chirp period other than the first, the two chirp signals can be written as

$$\bar{y}(t) = \begin{cases} \bar{s}(t) = \text{Re} \left[e^{2\pi i (f_1 t + \frac{B}{2T} t^2)} \right], & \text{for } t \in [0, T] \\ \text{Re} \left[e^{2\pi i (f_1 (t+T-\Delta t) + \frac{B}{2T} (t+T-\Delta t)^2)} \right], & \text{for } t \in [0, \Delta t] \\ \text{Re} \left[e^{2\pi i (f_1 (t-\Delta t) + \frac{B}{2T} (t-\Delta t)^2)} \right], & \text{for } t \in [\Delta t, T] \end{cases} \quad (11)$$

so that $\bar{\chi}(t)$ is:

$$\bar{\chi}(t) = \bar{y}(t) \cdot \bar{s}(t) = \begin{cases} \frac{1}{2} \text{Re} \left\{ e^{-2\pi i [f_1 \Delta t - \frac{B}{2T} \Delta t^2]} \cdot e^{2\pi i \frac{B}{T} t \Delta t} \right\} + \frac{1}{2} \text{Re} \left\{ e^{4\pi i [f_1 t + \frac{B}{2T} t^2]} \cdot e^{2\pi i [-f_1 \Delta t + \frac{B}{2T} \Delta t^2]} \cdot e^{-2\pi i \frac{B}{T} t \Delta t} \right\}, & \text{for } t \in [0, \Delta t] \\ \frac{1}{2} \text{Re} \left\{ e^{-2\pi i [f_1 \Delta t - \frac{B}{2T} \Delta t^2]} \cdot e^{2\pi i \frac{B}{T} t \Delta t} \right\} + \frac{1}{2} \text{Re} \left\{ e^{4\pi i [f_1 t + \frac{B}{2T} t^2]} \cdot e^{2\pi i [-f_1 \Delta t + \frac{B}{2T} \Delta t^2]} \cdot e^{-2\pi i \frac{B}{T} t \Delta t} \right\}, & \text{for } t \in [\Delta t, T] \end{cases} \quad (12)$$

Equation (12) shows that $\bar{\chi}(t)$ is the superposition of (i) a sinusoidal low-frequency signal and (ii) that of a chirp signal in both the intervals $[0, \Delta t]$ and $[\Delta t, T]$. For $t \in [0, \Delta t]$, the frequency of the sinusoidal signal is Δf_B , while for $t \in [\Delta t, T]$, the frequency of the sinusoidal signal is Δf_A . Thus, the *TOF* can be retrieved by applying the Fourier analysis on $\bar{\chi}(t)$ and then measuring the frequency value at which the peak of the sinusoidal low-frequency signal happens, provided that (i) and (ii) are nonoverlapping in their frequency.

Hence, the FMCW measurement protocol consists of (1) mixing the input and output signals $\bar{y}(t)$ and $\bar{s}(t)$, (2) filtering the mixer output $\bar{\chi}(t)$ with a low-pass filter to remove the high-frequency chirp component, (3) converting the resulting signal into a digital one $\bar{\chi}[n]$ via the ADC, (4) calculating the DFT of $\bar{\chi}[n]$, and then estimating the frequency value for which the highest peak in frequency is met via

$$\Delta f = \underset{n}{\text{argmax}} [DFT(\bar{\chi}[n])]. \quad (13)$$

The *TOF* is then obtained by substituting Equation (1) into Equation (13):

$$\Delta f = k_f \Delta t = \frac{B}{T} \cdot 2 \cdot \frac{d}{c} \quad \longrightarrow \quad TOF = \frac{T}{B} \Delta f. \quad (14)$$

It should be noted that the presence of the two “complementary” beat frequencies for each period leads to an ambiguity in *TOF* estimation, so that Δf can be either Δf_A or Δf_B depending on Δt being smaller or larger than $\frac{T}{2}$. This is because the two different delay values, Δt and $\Delta t' = T - \Delta t$, give the same $DFT(\bar{\chi}[n])$. Thus, T must be chosen so that the maximum expected delay/distance obeys $\Delta t_{max} < \frac{T}{2}$ so that the *TOF* can be unambiguously retrieved by using Equation (13). Under this constraint, and for a fixed inspection range, the PuC approach guarantees a double repetition rate with respect FMCWs. As an example, Figure 5 shows the $DFT(\bar{\chi}[n])$ obtained for the same distances shown for the PuC case. Note that $\Delta t_{max} < \frac{T}{2}$, hence $d3$ is out of the current measurement range.

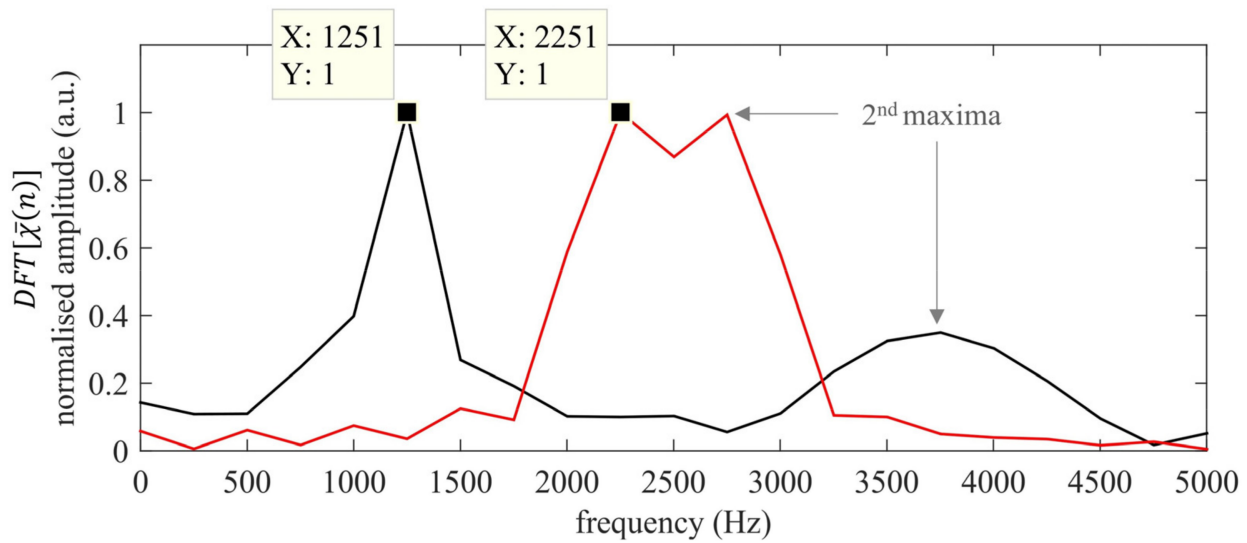


Figure 5. $ABS(DFT(\bar{\chi}[n]))$ obtained by simulating reflectors at $d_1 = 300$ mm (black) and $d_2 = 600$ mm (red).

Using Equation (14), a $ToF_{d_1}^{FMCW}$ and $ToF_{d_2}^{FMCW}$ equal in value to 1.000 ms and 1.800 ms are obtained respectively, which in turn correspond to distances of 343.27 mm and 617.67 mm. A first comparison of the estimated distance values for both the FMCWs and the correlation strategies shows that the latter approach results in better estimates, and this is in line with what has been shown in several research works [52,58]. However, the FMCW-based approach outputs good results, and these can be useful in several different ranges and positioning applications, especially when low hardware resources are available/needed, as is true for the present case. In fact, note that the beating frequencies values can be faithfully captured even with lower f_{ADC} values, thus relaxing (even more) the requested hardware feature.

3.4. Limits of the FMCW Approach and the Proposed FMCW-Modified Scheme

The estimated values of $ToF_{d_1}^{FMCW}$ and $ToF_{d_2}^{FMCW}$ suggest that the lower the real-time TOF to be estimated, the higher the relative error. In fact, for $\Delta t < \frac{1}{B}$, $\Delta f = \frac{B}{T}\Delta t < \frac{1}{T} = f_{REP}$, meaning that the low-frequency interference term does not complete a whole cycle within the excitation period T . This, in turn, hampers the correct measurement of Δf . For the current setup, B is equal to 5 kHz, and thus any Δt value that is less than 0.2 ms is below the FMCW resolution. Note that this value corresponds to a critical distance range of 0–68.6 mm in air.

In order to overcome this limitation, a modified FMCW-based measurement scheme is proposed here. This relies on simply using a shifted replica, $\bar{s}(t + t_0)$, of the input signal, $\bar{s}(t)$, for the mixing stage. This strategy allows for obtaining a $\Delta f > f_{REP} \forall \Delta t$ provided that $t_0 > \frac{1}{B}$, thus assuring at least a whole interference period is to be completed for T . The procedure is reported in Equation (15) for a single excitation period so as to be easily comparable to the standard FMCW approach, as per Equation (12):

$$\bar{\chi}(t) = \bar{y}(t) \cdot \bar{s}(t + t_0). \quad (15)$$

In order to gain more insight into the proposed procedure, $\bar{y}(t)$ is simulated to be the output ultrasonic signal coming from a reflector at a distance $d = 50$ mm, i.e., within the Δt 's critical range $< \frac{1}{B}$. Figure 6a shows both $\bar{s}(t)$ and $\bar{s}(t + t_0)$ in the first 0.4 ms of the 4 ms overall duration, while the corresponding $\bar{\chi}(t)$ and the resultant $DFT(\bar{\chi}[n])$ values are depicted in Figure 6b. Here, t_0 was chosen to be 0.2 ms, i.e., exactly equal in value to the critical $\frac{1}{B}$ bound. This simple example shows the potential of the proposed approach for the accurate estimation of distances < 68.6 mm; the modified approach completes a whole

interference cycle within the chirp period (Figure 6b, red plot), while the same is not true for the standard FMCW (Figure 6a, black plot). It is worth noting that this modified scheme can be easily implemented by storing a shifted replica of the input signal in the second available AWG buffer.

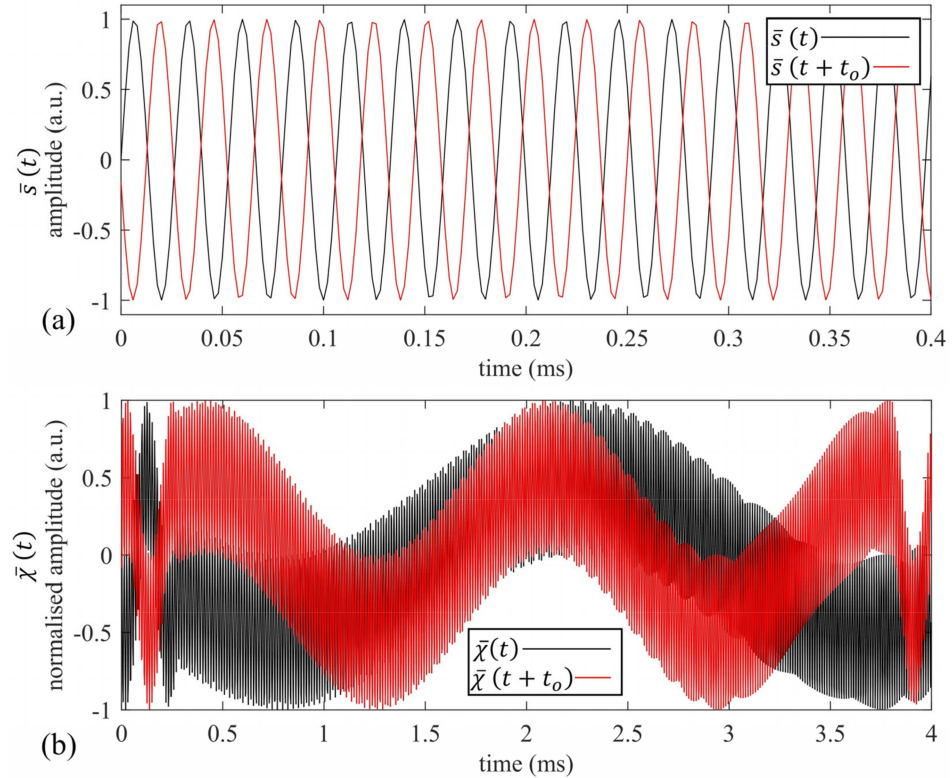


Figure 6. (a) A zoom of the $\bar{s}(t)$ (black) and $\bar{s}(t+t_0)$ signals (red); (b) $\bar{\chi}(t)$ (black) and $\bar{\chi}(t+t_0)$ for the simulated target distance of 50 mm.

4. Details of the Numerical Simulations and Figures of Merit

A MATLAB routine has been established to compare the capabilities of the correlation- and the two FMCW-based approaches to estimate the different TOF values and hence the measurement of different distances, d , in air. In particular, two chirp signals, having $T = 4$ ms, $B = 5$ kHz, and $f_c = 40$ kHz, were generated at $f_{DAQ} = f_{ADC} = 500$ kHz and sent together so as to have a periodic excitation. Note again that the chosen T value matches the maximum available samples of the Analog Discovery 2 device and that the characteristics of the chirps match those of the chosen transducers.

In order to consider the constraints of the FMCW-based approaches, a maximum measurable distance range of $\frac{T}{2} \times c \cong 680$ mm has been simulated. The signals $\bar{y}[n]$ and $\bar{\chi}[n]$ have been simulated by generating a signal $\bar{s}[n] \sim \bar{s}(t)$ at f_{DAQ} and then also generating a $\bar{y}[n]$ signal with the same rate and with $N_{\Delta t} = 201$ different Δt delays linearly-distributed in the interval $\Delta t \in [0, T/2)$ so as to sweep the range of distances $d \in [0, 680)$ mm at increasing increments of 3.4 mm. Note also that a $\bar{s}(t+t_0)$ has been generated for the modified FMCW-based approach in the same way, whereby the nonzero phase shift has been chosen to be $t_0 = 1/B = 0.2$ ms.

In order to simulate the effect of noise, $N_{trials} = 5000$ AWGN noise patterns were generated at f_{ADC} and added to $\bar{y}[n]$ to finally obtain $\bar{y}[n] \sim \bar{y}(t)$ and $\bar{\chi}[n] \sim \bar{\chi}(t)$. Five different noise power values were simulated corresponding to SNR = 40, 20, 0, -20, and -40 dB, where $SNR = 10 \log\{EN(\bar{y}[n])/EN(\bar{e}[n])\}$ and EN stands for the signal energy. Two different antialiasing low-pass filters (LPF1 and LPF2, see Figure 7b) were also applied using the command `filtfilt` to leave the resulting signal phases unaltered, with cut-off frequencies of $f_{c1} = 1.22 f_2$, $f_{c2} = 1.15 B$, respectively. Then, $\bar{y}[n]$ and $\bar{\chi}[n]$ were retrieved by

sampling the resulting signals at f_{ADC} . A sketch of the implemented routine is depicted in Figure 7a, while Figure 7b shows the implemented signal processing for each of the explored algorithms.

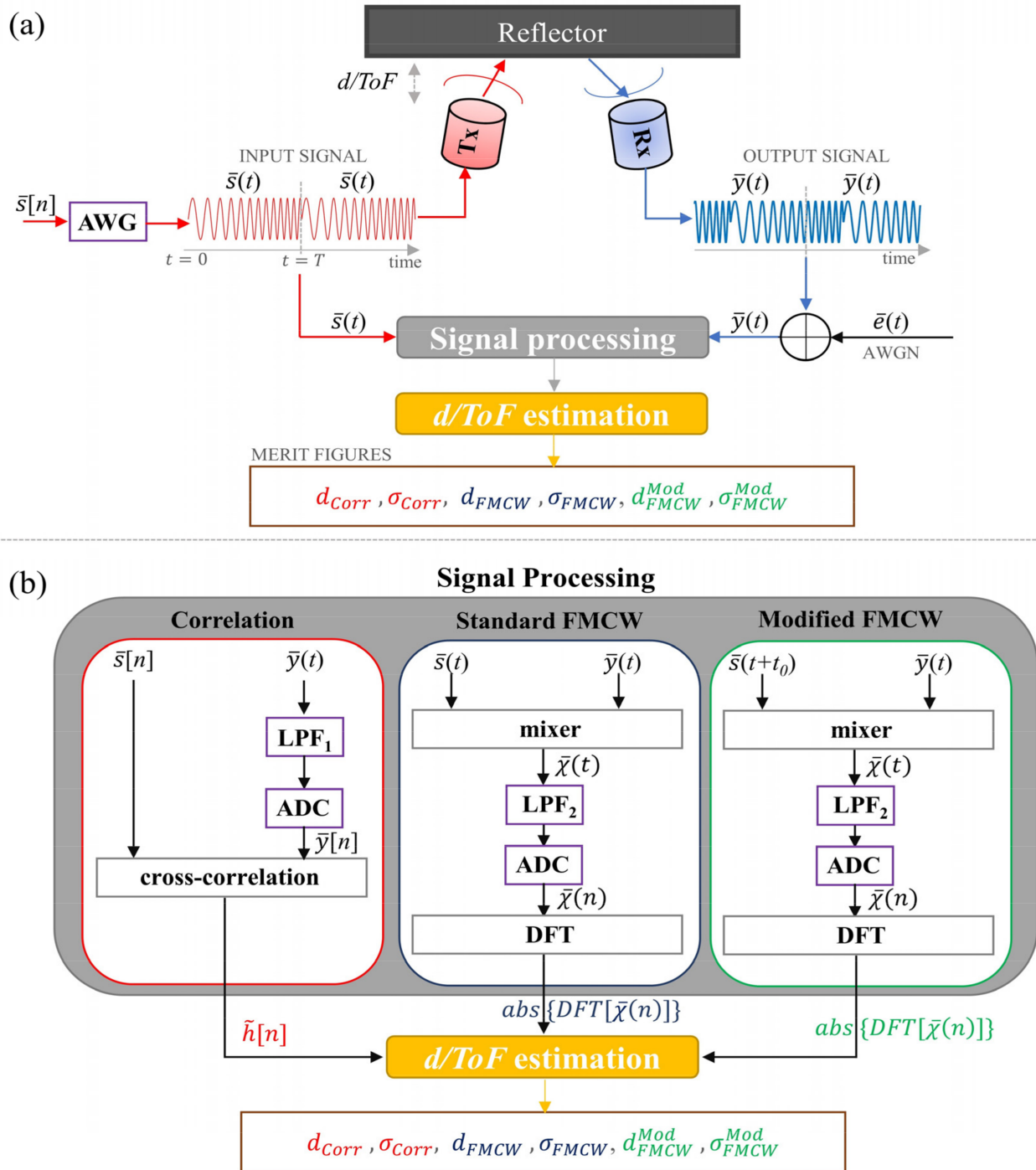


Figure 7. (a) Sketch of the implemented routine and retrieved figures of merit; (b) details of the implemented postprocessing for each of the three estimation methods.

As shown in Figure 7, two figures of merit were calculated for each scheme and SNR value in order to evaluate both the accuracy and the repeatability of distance estimation. In particular, the mean of the estimated d values was calculated over the N_{trials} , i.e., d_{Corr} , d_{FMCW} , and d_{FMCW}^{Mod} , respectively, for the correlation, standard, and modified FMCW schemes so as to evaluate the accuracy of each estimator. Additionally, a best fit

line was calculated for each dataset so as to compute the overall standard deviations: σ_{Corr} , σ_{FMCW} , and σ_{FMCW}^{Mod} . By assuming an underlying Gaussian distribution, the standard deviations allow for assessing the repeatability of each measurement scheme with a 68.3% probability of confidence [59].

5. Results and Discussion

5.1. Numerical Results

Figure 8a–e depict the estimated d_{Corr} , d_{FMCW} , and d_{FMCW}^{Mod} values with respect to the true simulated distances. It can be noticed from Figure 8a that all the methodologies fail to estimate the real distances at a very low SNR value, i.e., -40 dB. This is expected when choosing such narrowband transducers and relatively low f_{ADC} values and signal time durations. At an SNR level equal in value to -20 dB (see Figure 8b), the correlation output tracks the real distances well, although misleading results are evident at very low distances, and those obtained using the standard and the modified FMCW approach outputs are completely out of range.

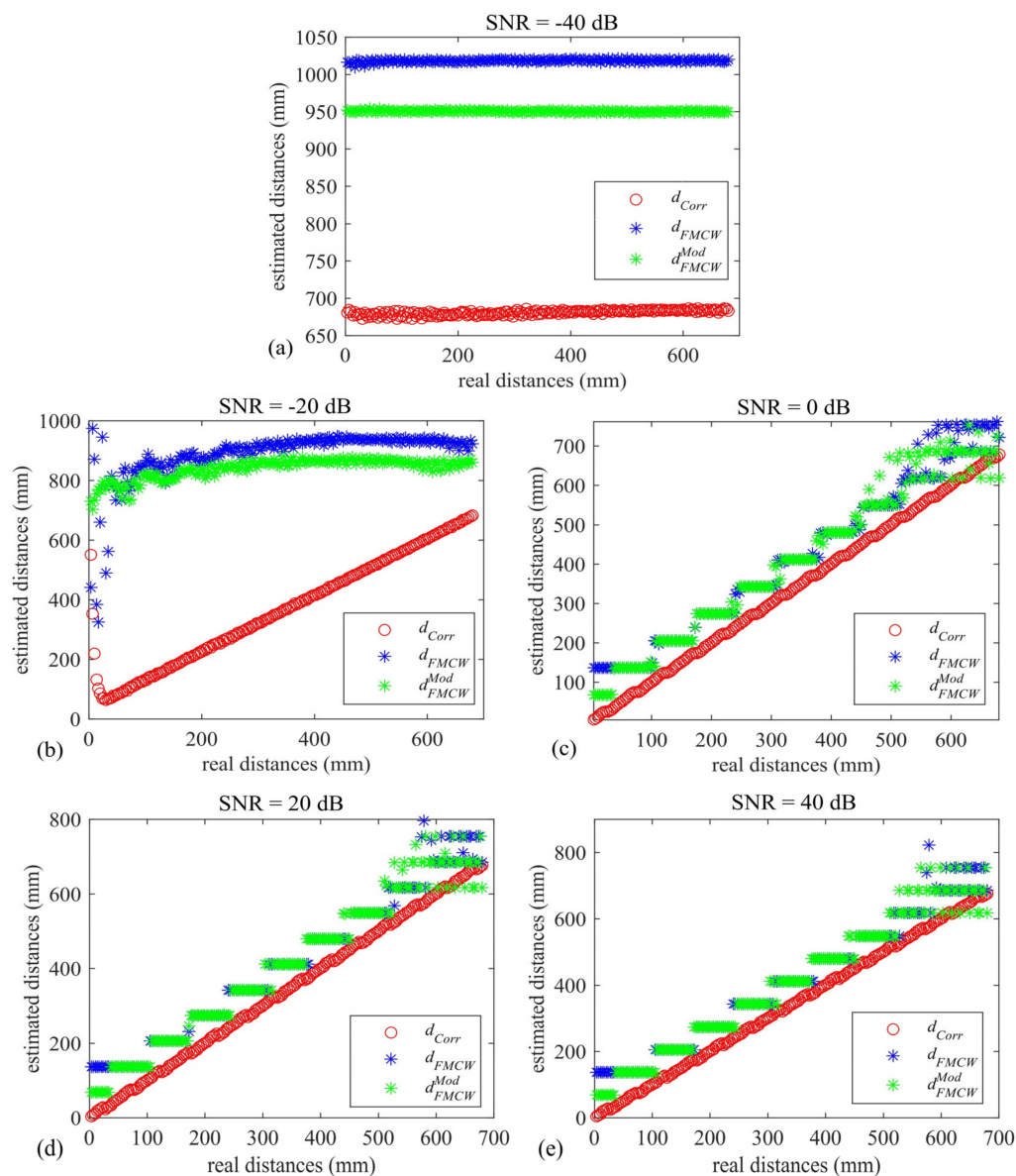


Figure 8. Estimated mean distance values vs. real distances for the correlation—(red circles), standard FMCW—(blue stars), and modified FMCW-based (green) star approaches at (a) -40 dB, (b) -20 dB, (c) 0 dB, (d) 20 dB, and (e) 40 dB.

For increasing the values of SNR (see Figure 8c–e), all the techniques estimate the real distances very well, with the highest accuracy given by the correlation method, as expected. It can be seen that the modified FMCW approach estimates distances <50 mm slightly better with respect to what is achievable with the standard FMCW; a narrower distribution of the modified FMCW plot (green-starred) with respect to the standard FMCW is visible at distances < 100 mm. It is worth noting that the modified FMCW agrees well with the standard FMCW results across the whole inspected range, thus leaving the range estimation capability unaltered. In order to evaluate the repeatability of each of the employed schemes, Table 2 reports the value of the total standard deviation σ_{Corr} , σ_{FMCW} , and σ_{FMCW}^{Mod} in millimeters for each of the SNR values, except for -40 dB. It can be seen that the repeatability of both the FMCW approaches tends toward that of the correlation approach as the SNR increases.

Table 2. Computed standard deviations for each estimator and SNR value, considering the results shown in Figure 8.

		SNR (dB)				
		-40	-20	0	20	40
Total standard deviation (mm)	σ_{Corr}	-	9.47	9.63	9.62	9.62
	σ_{FMCW}	-	13.89	10.73	10.60	10.57
	σ_{FMCW}^{Mod}	-	12.50	10.59	10.54	10.55

In order to better appreciate the potential of the modified FMCW scheme, it is worth simulating a measurement scheme that is not constrained by the digital nature of the hardware, a good example being the analog output of a PLL in the frequency-demodulation configuration for estimating the beat frequency after the FMCW. The PLL can be simply implemented onto the UGVs, bypassing the DAC of the Analog Discovery. Note that the PLL is commonly implemented via a voltage-controlled oscillator (VCO), an operational amplifier (op-amp), and a low-pass filter; thus, it can be set up on UGVs and drones without affecting the intended cost/weight ratio. A possible way to simulate such a circuit is to apply a three-point parabolic fit to the estimated TOF, i.e., to the result of Equation (13), so as to mimic the continuous-analog behavior of the PLL.

The results of this procedure for the correlation and the FMCW-based methods are shown in Figure 9. Even though the results at low SNR values (Figure 9a,b) are similar to the noninterpolated ones, a dramatic enhancement in accuracy is noticed for the remaining simulated values. In particular, it can be seen that the modified FMCW scheme outperforms the range estimation capabilities of the standard one, especially for distances below 50 mm, following the correlation output across the whole measurement range very well, starting from 0 dB of SNR. This is highlighted in Figure 9e, whereby a subplot containing a zoom of the three techniques within the range 0–100 mm is reported. Note that the two FMCW-based approaches tend to output the same results after the critical range distance, i.e., $d > 68.6$ mm. The computed σ_{Corr} , σ_{FMCW} , and σ_{FMCW}^{Mod} after the interpolation are reported in Table 3. As expected, these are slightly lower than those achieved without the interpolation procedure, and they are consistent for the three evaluated techniques.

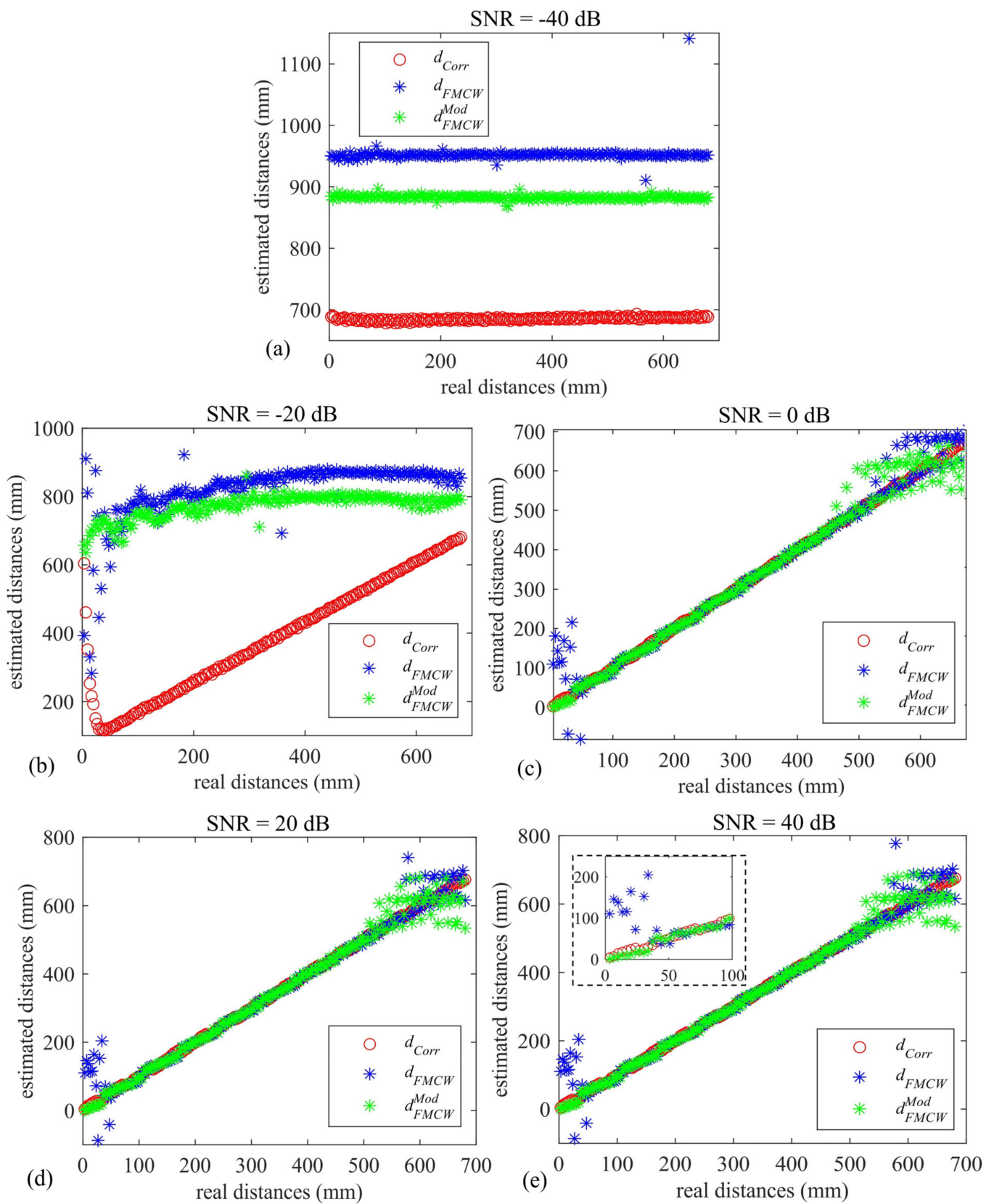


Figure 9. Estimated mean distance values vs. real distances for the correlation—(red circles), standard FMCW—(blue stars), and modified FMCW-based (green) star approaches at (a) -40 dB, (b) -20 dB, (c) 0 dB, (d) 20 dB, and (e) 40 dB, computed after a parabolic interpolation.

Table 3. Computed standard deviations for each estimator and SNR value, considering the results shown in Figure 9.

	SNR (dB)					
	−40	−20	0	20	40	
Total standard deviation (mm)	σ_{Corr}	-	9.40	9.62	9.61	9.61
	σ_{FMCW}	-	12.90	9.74	9.63	9.61
	σ_{FMCW}^{Mod}	-	11.54	9.61	9.55	9.56

5.2. Experimental Results

Experimental measurements were performed to corroborate the promising findings of the numerical simulations using the same hardware and chirp characteristics described in the previous sections. Figure 10 shows a photograph of the experimental setup. The two transducers were arranged as pulse-echo, with their closest sides being 15 mm away from each other. The transducers were originally placed in contact with a large reflector (i.e., at 0 mm), this being a 4 mm-thick aluminum plate, and were then moved further away from it by means of an in-house motorized scanning stage. The overall distance range was 0–100 mm in steps of 2 mm; a total of 100 measurements were recorded at each increment of distance so as to gain robust statistics. The signal generation, standard and modified FMCWs implementation with the three-point parabolic fitting, and stage movement were managed using a Virtual Instrument (VI) developed in LabVIEW. The measurements were carried out at room temperature, i.e., 20 °C, where the speed of sound in air was 343 ms^{−1}.

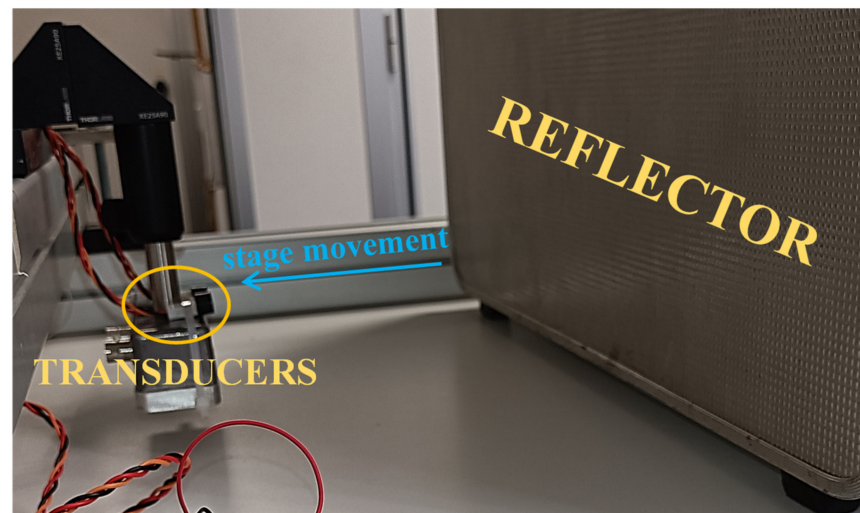


Figure 10. Photograph of the experimental setup.

Figure 11 shows the estimated distances obtained after the parabolic fit for both the standard (blue stars) and modified FMCWs (green stars), together with the actual distance, as the straight line in red, i.e., the ground truth. Note that the standard deviation values of the 100 measurements collected at each considered distance are also reported in the form of error bars. It can be seen that the modified FMCW shows improved performance with respect to its standard counterpart; the modified scheme follows the ground truth well along the whole range of distances considered. It is worth noting that crosstalk between the two transducers plays a detrimental role at distances below 10 mm from the reflector: see the relatively-large estimation error of the two FMCWs approaches within the range of distances 6–10 mm. However, this problem can be tackled by using a suitable amount of sound-absorbing material placed in between the two transducers. Nevertheless, the modified FMCW approach outputs satisfactory results within the mentioned short range

without employing any absorbing material, showing largely improved estimates for the 0 mm distance in both accuracy and repeatability with respect to the standard approach.

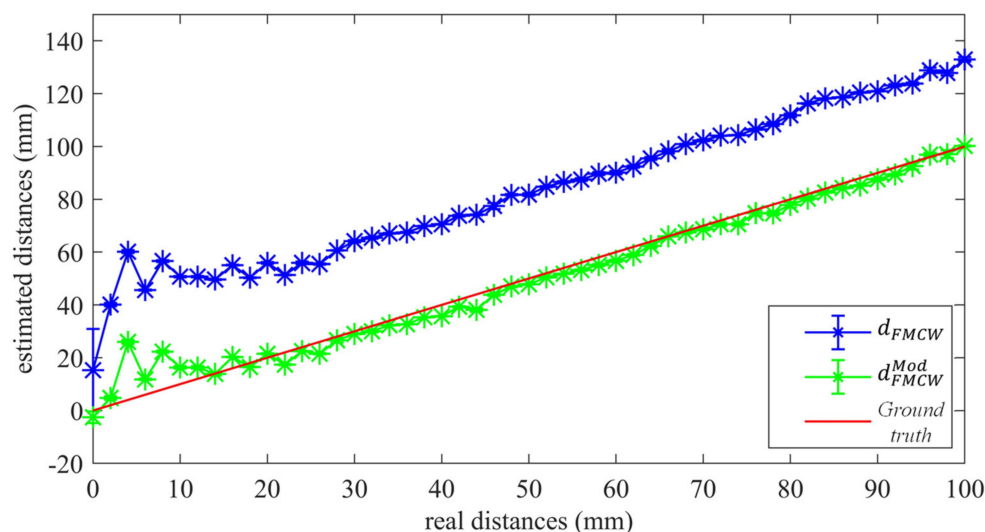


Figure 11. Experimental estimated distances and standard deviation values for both the standard (blue stars) and modified FMCW schemes, together with the ground truth (red line plot).

6. Conclusions and Future Work

An ultrasonic range and positioning system was investigated both numerically and experimentally to consider its possible application in unmanned ground vehicles. With this aim, the numerical simulations were taken into account for the features of an ultrasonic system, with a pair of low-frequency/narrowband ultrasonic transducers and an arbitrary waveform generator/digitizer, both of which are highly portable, light, and cheap.

A modified FMCW-based algorithm was introduced, and its capabilities for estimating distances in the range of 0–380 mm were numerically investigated, with particular emphasis on distances below 50 mm. This was carried out by comparing the proposed algorithm with both the widely-used correlation method and a standard FMCW counterpart.

The results showed that the proposed modified FMCW aids in estimating the distance to extremely near targets while leaving its estimation capabilities unaltered along a more extended inspection range. Finally, it must be noted that the proposed algorithm is of general validity for any value of transducer bandwidth, the choice of which will impose different limitations on the closest distances that can be estimated using the FMCW. A prototype of the proposed portable system implementing the modified FMCW scheme using a voltage-controlled oscillator for signal generation and a phase-locked loop to estimate the distance will be realized and set up on an unmanned ground vehicle in future work; its range estimation capabilities will be compared with other existing ranging and positioning schemes, such as MFSK. Its robustness regarding the Doppler effect will also be considered.

Author Contributions: Conceptualization, S.L., M.R. and M.M.; methodology, S.L., M.R. and M.M.; software, S.L. and M.R.; validation, S.L., M.R., M.M., D.A.H. and F.C.; formal analysis, S.L., M.R., M.M., D.A.H. and F.C.; investigation, S.L., M.R., M.M., D.A.H. and F.C.; resources, S.L., M.R., M.M., D.A.H. and F.C.; data curation, S.L. and M.R.; writing—original draft preparation, S.L. and M.R.; writing—review and editing, S.L., M.R., M.M., D.A.H. and F.C.; visualization, S.L.; project administration, S.L. and M.M.; funding acquisition, M.R. and F.C. All authors have read and agreed to the published version of the manuscript.

Funding: This research was funded by “Programma Operazione Nazionale e Innovazione 2014-2020, Fondo Sociale Europeo, Azione 1.2 “Attrazione e Mobilità Internazionale dei Ricercatori” —CUP: H24I19000410005”.

Data Availability Statement: The data presented in this study are available on request from the corresponding author.

Conflicts of Interest: The authors declare no conflict of interest.

References

1. Paredes, J.A.; Álvarez, F.J.; Aguilera, T.; Villadangos, J.M. 3D indoor positioning of UAVs with spread spectrum ultrasound and time-of-flight cameras. *Sensors* **2018**, *18*, 89. [[CrossRef](#)] [[PubMed](#)]
2. Liu, H.; Darabi, H.; Banerjee, P.; Liu, J. Survey of wireless indoor positioning techniques and systems. *IEEE Trans. Syst. Man Cybern. Part C Appl. Rev.* **2007**, *37*, 1067–1080. [[CrossRef](#)]
3. Gong, J.; Chang, T.H.; Shen, C.; Chen, X. Flight time minimization of UAV for data collection over wireless sensor networks. *IEEE J. Sel. Areas Commun.* **2018**, *36*, 1942–1954. [[CrossRef](#)]
4. Li, N.; Becerik-Gerber, B. Performance-based evaluation of RFID-based indoor location sensing solutions for the built environment. *Adv. Eng. Inform.* **2011**, *25*, 535–546. [[CrossRef](#)]
5. Anghel, A.; Vasile, G.; Cacoveanu, R.; Ioana, C.; Ciochina, S. Short-Range wideband FMCW radar for millimetric displacement measurements. *IEEE Trans. Geosci. Remote Sens.* **2014**, *52*, 5633–5642. [[CrossRef](#)]
6. Kittlaus, E.A.; Eliyahu, D.; Ganji, S.; Williams, S.; Matsko, A.B.; Cooper, K.B.; Forouhar, S. A low-noise photonic heterodyne synthesizer and its application to millimeter-wave radar. *Nat. Commun.* **2021**, *12*, 4397. [[CrossRef](#)]
7. Yang, B.; Yang, E. A Survey on Radio Frequency based Precise Localisation Technology for UAV in GPS-denied Environment. *J. Intell. Robot. Syst. Theory Appl.* **2021**, *103*, 38. [[CrossRef](#)]
8. Elloumi, W.; Guissous, K.; Chetouani, A.; Canals, R.; Leconge, R.; Emile, B.; Treuillet, S. Indoor navigation assistance with a Smartphone camera based on vanishing points. In Proceedings of the 2013 International Conference on Indoor Positioning and Indoor Navigation, IPIN 2013, Montbeliard, France, 28–31 October 2013.
9. Aguilar, W.G.; Salcedo, V.S.; Sandoval, D.S.; Cobeña, B. Developing of a Video-Based Model for UAV Autonomous Navigation. In Proceedings of the Communications in Computer and Information Science, Tianjin, China, 11–14 October 2017; Springer Verlag: Berlin/Heidelberg, Germany, 2017; Volume 720, pp. 94–105.
10. Aitenbichler, E.; Mühlhäuser, M. An IR local positioning system for smart items and devices. In Proceedings of the 23rd International Conference on Distributed Computing Systems Workshops, ICDCSW 2003, Providence, RI, USA, 19–22 May 2003; pp. 334–339.
11. Oh, J.H.; Kim, D.; Lee, B.H. An Indoor Localization System for Mobile Robots Using an Active Infrared Positioning Sensor. *J. Ind. Intell. Inf.* **2014**, *2*, 35–38. [[CrossRef](#)]
12. Kong, W.; Zhang, D.; Wang, X.; Xian, Z.; Zhang, J. Autonomous landing of an UAV with a ground-based actuated infrared stereo vision system. In Proceedings of the IEEE International Conference on Intelligent Robots and Systems, Tokyo, Japan, 3–7 November 2013; pp. 2963–2970.
13. Chen, L.H.; Wu, E.H.K.; Jin, M.H.; Chen, G.H. Intelligent fusion of wi-fi and inertial sensor-based positioning systems for indoor pedestrian navigation. *IEEE Sens. J.* **2014**, *14*, 4034–4042. [[CrossRef](#)]
14. Guo, X.; Elikplim, N.R.; Ansari, N.; Li, L.; Wang, L. Robust WiFi Localization by Fusing Derivative Fingerprints of RSS and Multiple Classifiers. *IEEE Trans. Ind. Inform.* **2020**, *16*, 3177–3186. [[CrossRef](#)]
15. Zhou, M.; Yuan, H.; Xie, L.; Tan, W.; Tian, Z. Mobile and redundant access point reduction for indoor unmanned aerial vehicle positioning using WLAN crowdsourcing fingerprints. *Phys. Commun.* **2019**, *36*, 100770. [[CrossRef](#)]
16. Oosterlinck, D.; Benoit, D.F.; Baecke, P.; Van de Weghe, N. Bluetooth tracking of humans in an indoor environment: An application to shopping mall visits. *Appl. Geogr.* **2017**, *78*, 55–65. [[CrossRef](#)]
17. Soria, P.R.; Palomino, A.F.; Arrue, B.C.; Ollero, A. Bluetooth network for micro-uavs for communication network and embedded range only localization. In Proceedings of the 2017 International Conference on Unmanned Aircraft Systems, ICUAS 2017, Miami, FL, USA, 13–16 June 2017; pp. 747–752.
18. Mainetti, L.; Patrono, L.; Sergi, I. A survey on indoor positioning systems. In Proceedings of the 2014 22nd International Conference on Software, Telecommunications and Computer Networks, SoftCOM 2014, Split, Croatia, 17–19 September 2014; pp. 111–120.
19. Koyuncu, H.; Yang, S.H. A survey of indoor positioning and object locating systems. *IJCSNS Int. J. Comput. Sci. Netw. Secur.* **2010**, *10*, 121–128.
20. Ijaz, F.; Yang, H.K.; Ahmad, A.W.; Lee, C. Indoor positioning: A review of indoor ultrasonic positioning systems. In Proceedings of the International Conference on Advanced Communication Technology, ICACT, PyeongChang, Korea, 27–30 January 2013; pp. 1146–1150.
21. Forouher, D.; Besselmann, M.G.; Maehle, E. Sensor fusion of depth camera and ultrasound data for obstacle detection and robot navigation. In Proceedings of the 2016 14th International Conference on Control, Automation, Robotics and Vision (ICARCV), Phuket, Thailand, 13–15 November 2016; pp. 1–6.
22. Kasprzyczak, L.; Pietrzak, R. Electromagnetic compatibility tests of Mining Mobile Inspection Robot. *Arch. Min. Sci.* **2014**, *59*, 427–439. [[CrossRef](#)]

23. Richards, M.A.; Scheer, J.A.; Holm, W.A. *Principles of Modern Radar: Basic Principles*; Richards, M.A., Melvin, W.L., Eds.; SciTech Pub.: Raleigh, NC, USA, 2010; ISBN 9781613531488.
24. De Simone, M.C.; Rivera, Z.B.; Guida, D. Obstacle avoidance system for unmanned ground vehicles by using ultrasonic sensors. *Machines* **2018**, *6*, 18. [[CrossRef](#)]
25. Lam, F.; Szilard, J. Pulse compression techniques in ultrasonic non-destructive testing. *Ultrasonics* **1976**, *14*, 111–114. [[CrossRef](#)]
26. Gan, T.H.; Hutchins, D.A.; Billson, D.R.; Schindel, D.W. The use of broadband acoustic transducers and pulse-compression techniques for air-coupled ultrasonic imaging. *Ultrasonics* **2001**, *39*, 181–194. [[CrossRef](#)]
27. Stove, A.G. Linear FMCW radar techniques. *IEE Proc. Part F Radar Signal Process.* **1992**, *139*, 343–350. [[CrossRef](#)]
28. Kunita, M. Range measurement in ultrasound FMCW system. *Electron. Commun. Jpn. Part III: Fundam. Electron. Sci.* **2007**, *90*, 9–19. [[CrossRef](#)]
29. Kunita, M.; Sudo, M.; Inoue, S.; Akahane, M. A new method for blood velocity measurements using ultrasound FMCW signals. *IEEE Trans. Ultrason. Ferroelectr. Freq. Control.* **2010**, *57*, 1064–1076. [[CrossRef](#)]
30. Svilainis, L.; Lukoseviciute, K.; Dumbrava, V.; Chaziachmetovas, A. Subsample interpolation bias error in time of flight estimation by direct correlation in digital domain. *Meas. J. Int. Meas. Confed.* **2013**, *46*, 3950–3958. [[CrossRef](#)]
31. Barshan, B. Fast processing techniques for accurate ultrasonic range measurements. *Meas. Sci. Technol.* **2000**, *11*, 45–50. [[CrossRef](#)]
32. Huang, S.S.; Huang, C.F.; Huang, K.N.; Young, M.S. A high accuracy ultrasonic distance measurement system using binary frequency shift-keyed signal and phase detection. *Rev. Sci. Instrum.* **2002**, *73*, 3671. [[CrossRef](#)]
33. Hazas, M.; Hopper, A. Broadband ultrasonic location systems for improved indoor positioning. *IEEE Trans. Mob. Comput.* **2006**, *5*, 536–547. [[CrossRef](#)]
34. Saad, M.M.; Bleakley, C.J.; Dobson, S. Robust high-accuracy ultrasonic range measurement system. In Proceedings of the IEEE Transactions on Instrumentation and Measurement, Hangzhou, China, 9–12 May 2011; Volume 60, pp. 3334–3341.
35. Jackson, J.C.; Summan, R.; Dobie, G.I.; Whiteley, S.M.; Pierce, S.G.; Hayward, G. Time-of-flight measurement techniques for airborne ultrasonic ranging. *IEEE Trans. Ultrason. Ferroelectr. Freq. Control.* **2013**, *60*, 343–355. [[CrossRef](#)]
36. Ronkin, M.V.; Kalmykov, A.A. Investigation of the time delay difference estimator for FMCW signals. In Proceedings of the CEUR Workshop Proceedings, Bloomington, IN, USA, 20–21 January 2017; Volume 2005, pp. 90–99.
37. Berkol, G.; Baltus, P.G.M.; Harpe, P.J.A.; Cantatore, E. A 2.67 μ j per Measurement FMCW Ultrasound Rangefinder System for the Exploration of Enclosed Environments. *IEEE Solid-State Circuits Lett.* **2020**, *3*, 326–329. [[CrossRef](#)]
38. De Angelis, A.; Moschitta, A.; Carbone, P.; Calderini, M.; Neri, S.; Borgna, R.; Peppucci, M. Design and characterization of a portable ultrasonic indoor 3-D positioning system. *IEEE Trans. Instrum. Meas.* **2015**, *64*, 2616–2625. [[CrossRef](#)]
39. Carotenuto, R. A range estimation system using coded ultrasound. *Sens. Actuators A Phys.* **2016**, *238*, 104–111. [[CrossRef](#)]
40. Natarajan, S.; Singh, R.S.; Lee, M.; Cox, B.P.; Culjat, M.O.; Grundfest, W.S.; Lee, H. Accurate step-FMCW ultrasound ranging and comparison with pulse-echo signaling methods. In Proceedings of the Medical Imaging 2010: Ultrasonic Imaging, Tomography, and Therapy, San Diego, CA, USA, 14–15 February 2010; Volume 7629, p. 76290D.
41. Laureti, S.; Khalid Rizwan, M.; Malekmohammadi, H.; Burrascano, P.; Natali, M.; Torre, L.; Rallini, M.; Puri, I.; Hutchins, D.; Ricci, M. Delamination detection in polymeric ablative materials using pulse-compression thermography and air-coupled ultrasound. *Sensors* **2019**, *19*, 2198. [[CrossRef](#)]
42. Burrascano, P.; Laureti, S.; Senni, L.; Ricci, M. Pulse Compression in Nondestructive Testing Applications: Reduction of Near Sidelobes Exploiting Reactance Transformation. *IEEE Trans. Circuits Syst. I Regul. Pap.* **2019**, *66*, 1886–1896. [[CrossRef](#)]
43. Solodov, I.; Bai, J.; Bekgulyan, S.; Busse, G. A local defect resonance to enhance acoustic wave-defect interaction in ultrasonic nondestructive evaluation. *Appl. Phys. Lett.* **2011**, *99*, 211911. [[CrossRef](#)]
44. Gedanken, A. Using sonochemistry for the fabrication of nanomaterials. *Ultrason. Sonochem.* **2004**, *11*, 47–55. [[CrossRef](#)]
45. Dai, J.C.; Bailey, M.R.; Sorensen, M.D.; Harper, J.D. Innovations in Ultrasound Technology in the Management of Kidney Stones. *Urol. Clin. North Am.* **2019**, *46*, 273–285. [[CrossRef](#)]
46. Nie, L.; Hutchins, D.A.; Astolfi, L.; Cooper, T.P.; Clare, A.T.; Adams, C.; Watson, R.L.; Thomas, P.J.; Cowell, D.M.J.; McLaughlan, J.R.; et al. A Metallic Additively-Manufactured Metamaterial for Enhanced Monitoring of Acoustic Cavitation-Based Therapeutic Ultrasound. *Adv. Eng. Mater.* **2021**, *24*, 2100972. [[CrossRef](#)]
47. Kesner, S.B.; Howe, R.D. Robotic catheter cardiac ablation combining ultrasound guidance and force control. *Int. J. Robot. Res.* **2014**, *33*, 631–644. [[CrossRef](#)]
48. Boctor, E.M.; Choti, M.A.; Burdette, E.C.; Webster, R.J. Three-dimensional ultrasound-guided robotic needle placement: An experimental evaluation. *Int. J. Med. Robot. Comput. Assist. Surg.* **2008**, *4*, 180–191. [[CrossRef](#)]
49. Khan, S.; Huh, J.; Ye, J.C. Adaptive and Compressive Beamforming Using Deep Learning for Medical Ultrasound. *IEEE Trans. Ultrason. Ferroelectr. Freq. Control.* **2020**, *67*, 1558–1572. [[CrossRef](#)]
50. Mercuri, M.; Liu, Y.H.; Lorato, I.; Torfs, T.; Wieringa, F.; Bourdoux, A.; Van Hoof, C. A Direct Phase-Tracking Doppler Radar Using Wavelet Independent Component Analysis for Non-Contact Respiratory and Heart Rate Monitoring. *IEEE Trans. Biomed. Circuits Syst.* **2018**, *12*, 632–643. [[CrossRef](#)]
51. Lykou, G.; Moustakas, D.; Gritzalis, D. Defending airports from UAS: A survey on cyber-attacks and counter-drone sensing technologies. *Sensors* **2020**, *20*, 3537. [[CrossRef](#)]

52. Battaglini, L.; Laureti, S.; Ricci, M.; Burrascano, P.; Davis, L.A.J.; Hutchins, D.A. The use of Pulse Compression and Frequency Modulated Continuous Wave to improve Ultrasonic Non Destructive Evaluation of highly-scattering materials. In Proceedings of the IEEE International Ultrasonics Symposium, IUS, Chicago, IL, USA, 3–6 September 2014.
53. Hutchins, D.; Burrascano, P.; Davis, L.; Laureti, S.; Ricci, M. Coded waveforms for optimised air-coupled ultrasonic nondestructive evaluation. *Ultrasonics* **2014**, *54*, 1745–1759. [[CrossRef](#)]
54. Misaridis, T.; Jensen, J.A. Use of modulated excitation signals in medical ultrasound. Part II: Design and performance for medical imaging applications. *IEEE Trans. Ultrason. Ferroelectr. Freq. Control.* **2005**, *52*, 192–206. [[CrossRef](#)] [[PubMed](#)]
55. Hutchins, D.A.; Watson, R.L.; Davis, L.A.J.; Akanji, L.; Billson, D.R.; Burrascano, P.; Laureti, S.; Ricci, M. Ultrasonic propagation in highly attenuating insulation materials. *Sensors* **2020**, *20*, 2285. [[CrossRef](#)] [[PubMed](#)]
56. Turin, G.L. An Introduction to Matched Filters. *IRE Trans. Inf. Theory* **1960**, *6*, 311–329. [[CrossRef](#)]
57. Tarbox, E.; Akhlaghi, N.; Dhawan, A.; Gammell, P.; Chitnis, P.; Sikdar, S. Low-power ultrasound imaging systems using time delay spectrometry. In Proceedings of the IEEE International Ultrasonics Symposium, IUS, Washington, DC, USA, 6–9 September 2017.
58. Battaglini, L.; Burrascano, P.; Ricci, M.; Senni, L. Ultrasonic Frequency Modulated Continuous Wave for Range Estimation. In *Ultrasonic Nondestructive Evaluation Systems*; Springer: Berlin/Heidelberg, Germany, 2015; pp. 297–320.
59. Battaglini, L.; Burrascano, P.; De Angelis, A.; Moschitta, A.; Ricci, M. A low-cost ultrasonic rangefinder based on frequency modulated continuous wave. In Proceedings of the 20th IMEKO TC4 Symposium on Measurements of Electrical Quantities: Research on Electrical and Electronic Measurement for the Economic Upturn, Together with 18th TC4 International Workshop on ADC and DCA Modeling and Testing, IWADC 2014, Benevento, Italy, 15–17 September 2014; pp. 1122–1126.